Journal of Alloys and Compounds 724 (2017) 820–826

Contents lists available at ScienceDirect

Journal of Alloys and Compounds

journal homepage: http://www.elsevier.com/locate/jalcom

Thermite synthesis, structural and magnetic properties of Co-Al_2O_3 nanocomposite films

V.G. Myagkov [a, *], L.E. Bykova [a], V.S. Zhigalov [a], A.A. Matsynin [a], M.N. Volochaev [a], I.A. Tambasov [a], Yu.L. Mikhlin [b], G.N. Bondarenko [b]

[a] Kirensky Institute of Physics, Federal Research Center KSC SB RAS, Krasnoyarsk, Russia
[b] Institute of Chemistry and Chemical Technology, Federal Research Center KSC SB RAS, Krasnoyarsk, Russia

ARTICLE INFO

Article history:
Received 27 February 2017
Received in revised form
18 June 2017
Accepted 8 July 2017
Available online 10 July 2017

Keywords:
Thermite reactions
Reactive films
Ferromagnetic nanocomposite films
Al_2O_3

ABSTRACT

We have synthesized ferromagnetic nanocomposite Co-Al_2O_3 thin films via a thermite reaction between Al and Co_3O_4 with layer geometry. The starting Al/Co_3O_4 bilayers were obtained by the deposition of Al layers onto Co_3O_4 films at room temperature and were annealed at temperatures between 50 and 700 °C at 50 °C intervals. Above ~450 °C the Co_3O_4 partially transformed into the CoO phase. The simultaneous solid-state reactions of Al with Co_3O_4 and Al with CoO started above the initiation temperature T_{in} ~500 °C, which did not depend on the bilayer thickness. After annealing at 700 °C about 60% of the Co was reduced by the Al and the rest of the Co was contained in intermediate $CoAl_2O_4$ shells, which separated the Co nanoparticles from the Al_2O_3 matrix. Above 700 °C the reaction was complete and the final products were noninteracting Co nanoparticles with an average size of ~40 nm enveloped by $CoAl_2O_4$ shells, which embedded into a dielectric Al_2O_3 matrix. The synthesized Co-Al_2O_3 nanocomposite films possessed soft magnetic behavior and good chemical stability.

1. Introduction

Nanoenergetic materials are a new class of energetic composites comprising of fuel and oxidizer particles decreased to nanoscale dimensions. In contrast to traditional energetic materials the nanomaterials have high interfacial contact areas, which decreases the diffusion distances between reactants and as a result the nanoenergetic materials have lower ignition temperatures T_{ig}, low ignition delay, an enhanced rate of energy release and a significant increase in the combustion velocity to 1 km/s [1–6]. Thermites comprising of nano-sized fuels such as Al, Mg, Ta, Ti, Zr and oxidizers such as SnO_2, WO_3, MoO_3, CuO, Bi_2O_3, I_2O_5, Cr_2O_3, Fe_2O_3 are termed nanostructured metastable intermolecular composites, nanothermites or superthermites, and have been widely investigated as a subclass of nanoenergetic materials. Among the several types of nanoenergetic materials, multilayer nanofilms, consisting of alternating layers of reactants, have attracted great interest over the last two decades because they presented a simple model for both theoretical and experimental study of atomic transfer across an interface for the fundamental understanding of reaction mechanisms at the nanoscale [7–15]. Free-standing multilayer nanofilms above the ignition temperature T_{ig} have a self-propagating high-temperature synthesis (SHS) mode, because the heat release at the reaction front exceeds the heat loss from the unreacted regions of the film. Below T_{ig} the reaction does not have an SHS mode and occurs by the slow intermixing of the reactive layers across interfaces. When the sample temperature decreases below the initiation temperature T_{in} of the reaction the heat release becomes negligible and leads to the complete termination of the reaction. In contrast to free-standing multilayer nanofilms, the combustion wave for reactive bilayer films coupled with a substrate, which is the major heat sink during a reaction, occurs when the temperature of a sample T_S exceeds the initiation temperature T_{in} ($T_S > T_{in}$) and the heating rate is higher than 20 K/s. At heating rates less than 20 K/s the reaction occurs by low reactive diffusion across the entire interface [16,17].

In our previous works, we demonstrated a new synthesis of ferromagnetic Fe-In_2O_3 [16], Fe-ZrO_2 [17] and Co-ZrO_2 [18] nanocomposite films using thermite reactions in In/Fe_2O_3, Zr/Fe_2O_3 and Zr/Co_3O_4 bilayers, respectively. The thermite method opens the door to a facile and highly efficient method for the fabrication of a wide variety of functional nanocomposite films, containing metallic

* Corresponding author.
E-mail address: miagkov@iph.krasn.ru (V.G. Myagkov).

http://dx.doi.org/10.1016/j.jallcom.2017.07.081
0925-8388/

clusters embedded into an oxide matrix.

Many methods have been used to synthesize granular nanocomposite films, such as co-sputtering [19–21], radio frequency magnetron sputtering [22,23], pulsed laser deposition [24,25], ion-beam sputtering [26,27], sol-gel method [28], etc. These composite films possess promising physicochemical properties which strongly depend on the method of preparation, the particle size, the concentration and the chemical bonding between the nanoparticles and the matrix. In particular, nanogranular $Co_{0.55}$-$(Al_2O_3)_{0.45}$ films possess superferromagnetic ordering and a growth-induced perpendicular anisotropy [27], granular Co-Al_2O_3 thin films have shown spin depended tunneling [21] and tunnel-type giant magnetoresistance [29] and characteristic features of spin accumulation in Co nanoparticles [30] have been observed in Co-Al-O granular films.

In this paper, we present a complete study of the preparation and structural characterization of granular nanocomposite Co-Al_2O_3 films obtained by using a thermite reaction (1) in Al/Co_3O_4 bilayers:

$$3Co_3O_4 + 8Al \rightarrow 4Al_2O_3 + 9Co \quad (1)$$

The fabricated Co-Al_2O_3 nanocomposite films are characterized by X-ray diffraction, transmission electron microscopy and electrical and magnetic investigations. The aim of this contribution is to analyze the solid-state thin-film reaction between Al and Co_3O_4 and to find the correlation between the magnetic and electrical properties of Co-Al_2O_3 nanocomposites and their structural features.

2. Experimental

2.1. Synthesis

Fig. 1a shows a schematic diagram of the thermite synthesis of Co-Al_2O_3 nanocomposite films. It consists of the deposition of a Co layer on a glass substrate, subsequent oxidation of Co into Co_3O_4, the deposition of Al film on the top Co_3O_4 layer and subsequent annealing at different temperatures (up to 700 °C). The initial films were obtained by the thermal deposition of Co layers at a temperature of 250 °C onto NaCl (001) and chemically pure glass substrates having a thickness of 0.18 mm in a vacuum at a residual pressure of 10^{-6} Torr. Previously, the substrates were degassed at 350 °C for 1 h. The Co_3O_4 films were obtained by the oxidation of the initial Co films at a temperature of ~350 °C in an air environment. The top Al layer was deposited at room temperature to prevent a reaction between the Al and Co_3O_4 during the deposition. The initial Al/Co_3O_4 bilayers, with an approximate stoichiometry of Co:Al = 1:1, were used in these experiments. Films of Al/Co_3O_4/NaCl (001) with thicknesses of Co equal to 20 nm and Al - 30 nm were prepared for transmission electron microscopy (TEM) studies. The obtained Al/Co_3O_4 films were separated from the substrate, placed on molybdenum TEM grid and annealed at 700 °C for 1 h. The morphology and chemical composition of the films were investigated by TEM using a JEOL JEM-2100, equipped with an energy-dispersive spectrometer (EDS) Oxford INCA X-sight, at an accelerating voltage of 200 kV. Films on glass substrates with total thicknesses of 300–400 nm were used in the rest of the experiments. The starting Al/Co_3O_4 bilayers for magnetic, electrical and TEM studies were annealed at temperatures between 50 and 700 °C at 50 °C intervals. The samples were held at each temperature for 1 h. All the synthesized Co-Al_2O_3 samples were annealed at a pressure of 10^{-6} Torr.

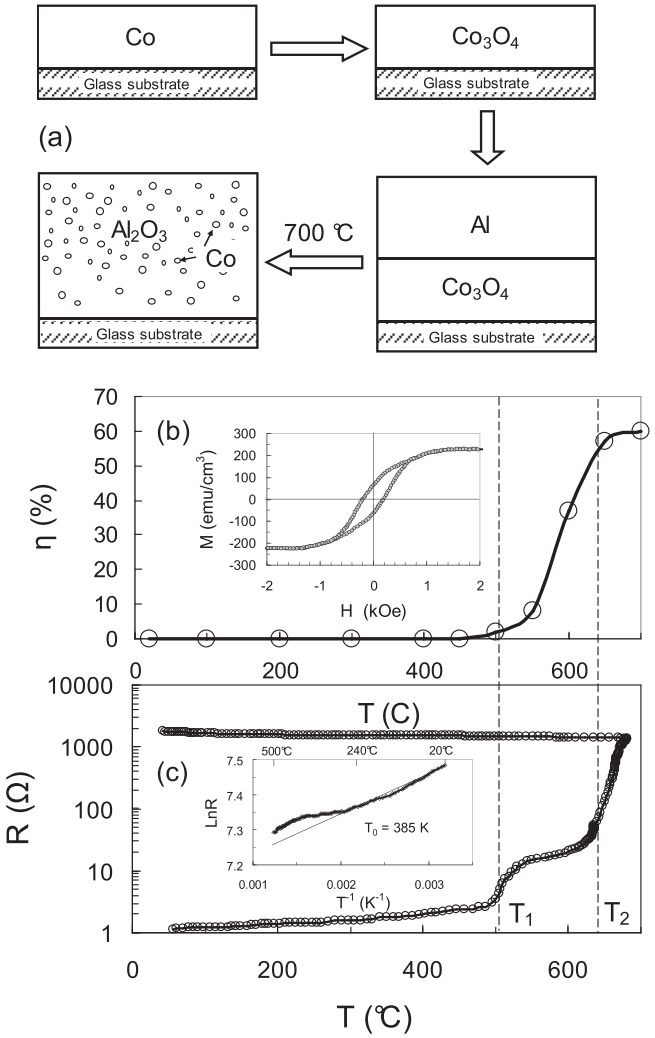

Fig. 1. (a) Schematic diagram of the thermite synthesis of Co-Al_2O_3 nanocomposite films. (b) The degree of Co reduction η as a function of annealing temperature T for the Al/Co_3O_4 bilayers. The inset shows the room temperature hysteresis loop of the synthesized Co- Al_2O_3 nanocomposite after annealing at 700 °C. (c) Electrical resistance of the Al/Co_3O_4 bilayers heated up to 700 °C as a function of temperature measurement T. The inset shows the ln R vs T^{-1} plot for the as-synthesized Co- Al_2O_3 sample after cooling in the 700 °C - 25 °C temperature interval.

2.2. Characterization

The phases formed during the synthesis process were identified using a DRON-4007 X-ray diffractometer (Cu Kα radiation). The thicknesses of the Al and Co_3O_4 layers were determined via X-ray fluorescent analysis. The saturation magnetization M_S, in-plane hysteresis loops and magnetic moment of the samples were measured by a vibrating magnetometer and were also controlled by torque measurements which have been described in detail in our previous work [18]. As is previously known, all Co oxides are non-magnetic at room temperature. To find the Co reduction degree $\eta(T_S)$ as a function of the annealing temperature T_S the magnetic moment $M_S^{Co}V_0$ of the initial (prior to oxidation) Co film with V_0 volume was measured. The degree of Co reduction $\eta(T_S)$ was obtained using Formula (2):

$$\eta\,(T_S) = M_S^{Co}V(T_S)/M_S^{Co}V_0 = V(T_S)/V_0, \quad (2)$$

where $V(T_S)$ is the Co reduction volume after annealing at

temperature T_S.

Formula (2) indicates that the total reduction of Co corresponds to $\eta = 100\%$ and $\eta = 0$ if reaction (1) does not occur. The resistance was measured by using the standard four-probe technique in a vacuum of 10^{-6} Torr. The plot of resistance $R(T_S)$ as function of the temperature T_S was carried out by heating an as-deposited Al/Co_3O_4 sample from room temperature to 700 °C with a constant heating rate of 4 °C/min and then cooling at a rate of ~3 °C/min to room temperature. The magnetic properties were examined using a vibrating magnetometer with an applied field of 2 kOe at room temperature.

3. Results

3.1. Starting Al/Co_3O_4 bilayers characterization

The initial Co films had a saturation magnetization ($M_S^{Co} = 1400$ emu/cm^3) coinciding with the saturation magnetization of the bulk samples. The samples were oxidized in air for the formation of a Co_3O_4 phase which had zero magnetization. To avoid a reaction between the Al and Co_3O_4, the starting Al/Co_3O_4 bilayers were obtained from the deposition of the Al layer onto the Co_3O_4 film at room temperature. The magnetization M_S of the samples did not increase after the deposition of the Al layer.

3.2. Temperature characterization of the Al/Co_3O_4 reaction

Fig. 1b, c shows the degree of Co reduction $\eta(T_S)$ and the electrical resistance $R(T_S)$ as a function of the annealing temperature T_S for the Al/Co_3O_4 bilayers. Up to ~500 °C the saturation magnetization M_S of the Al/Co_3O_4 bilayers remained equal to zero ($\eta = 0$), which indicated that there was no mixing and no reaction between the Al and Co_3O_4 layers. As the annealing temperature increased above T_1 ~ 500 °C, the reduction degree η slowly increased until T_2 ~ 650 °C and afterwards strongly increased until 700 °C, reaching a maximum of η ~60% at 700 °C (Fig. 1b). It follows from this that Reaction (1) has an initiation temperature $T_{in} = T_1$ ~ 500 °C. The reduction degree η slowly increased up to the characteristic temperature T_2 ~ 650 °C, and above this temperature the reduction degree η strongly increased up to 60% at 700 °C, which indicates that more than 60% of the Co was reduced by the Al. Fig. 1c shows the electrical resistance $R(T_S)$ as a function of the annealing temperature T_S for the Al/Co_3O_4 bilayers which were heated at a rate of 4 °C/min to 700 °C and then cooled to room temperature. The temperature increase above $T_1 = T_{in}$ ~500 °C led to a slow increase of the electrical resistance until T_2 ~ 650 °C and was followed by a rapid increase until 700 °C, which was due to the initiation and development of Reaction (1) at T_{in} = 500 °C. Above 700 °C the resistance is virtually unchanged. Cooling the samples to room temperature resulted in an increase of the resistance, which is a typical feature of semiconductor resistance.

Undoubtedly, the rapid increase of the electrical resistance above T_1 ~ 500 °C was associated with the formation of the insulating Al_2O_3 matrix. Above 700 °C the electrical resistance and the reduction degree η increased insignificantly which suggests that the reaction between Al and Co_3O_4 was basically completed at 700 °C. The electrical resistance $R(T_S)$ (Fig. 1c) and reduction degree $\eta(T_S)$ (Fig. 1b) clearly point to the existence of structural features in the temperature interval between 500 °C and 600 °C, which will be discussed below.

3.3. XRD characterizations

The diffraction pattern of the initial Al/Co_3O_4 bilayers contained reflections from the polycrystalline Al and Co_3O_4 phases (Fig. 2a). After annealing at 450 °C the Al and Co_3O_4 reflections decreased and new peaks for the CoO phase were formed (Fig. 2b); that is the start of reaction (3). After annealing at 600 °C reflections from Co_3O_4 disappear and new (111), (200) peaks of the cubic phase of fcc-Co arise (Fig. 2c). An insignificant increase in the intensity of the Al(200) peak can be a result of the reorientation of the Al grain structure to the (200) orientation by annealing. The lack of Co_3O_4 and the diminution of the Al and CoO peaks implies the continuation of the decomposition of Co_3O_4 due to reaction (3). The solid-state reactions between Co_3O_4 and Al (2), and between Al and CoO (4) start simultaneously in the Al/Co_3O_4 bilayers after annealing at 500 °C.

$$2\,Co_3O_4 \rightarrow 6\,CoO + O_2 \quad (3)$$

$$3CoO + 2Al \rightarrow 3\,Co + Al_2O_3 \quad (4)$$

After annealing at 700 °C only the (111) and (200) reflections from the high-temperature fcc-Co phase remain and there are no peaks from the stable low-temperature hexagonal hcp-Co and Al_2O_3 phases (Fig. 2d). As is previously known, the metastable fcc-Co phase is often stabilized in thin films and nanostructures. However, the existence of hcp-Co cannot be excluded due to the overlap with the fcc-Co diffraction reflections. Al_2O_3. This suggests the growth of Co grains as the annealing temperature increases up 700 °C and thus the finished reaction products are polycrystalline Co grains embedded into an amorphous Al_2O_3 matrix.

The rapid increasing of the electrical resistance was associated with the formation of the insulating Al_2O_3 matrix; this proves that the volume fraction of the metallic Co phase is below the

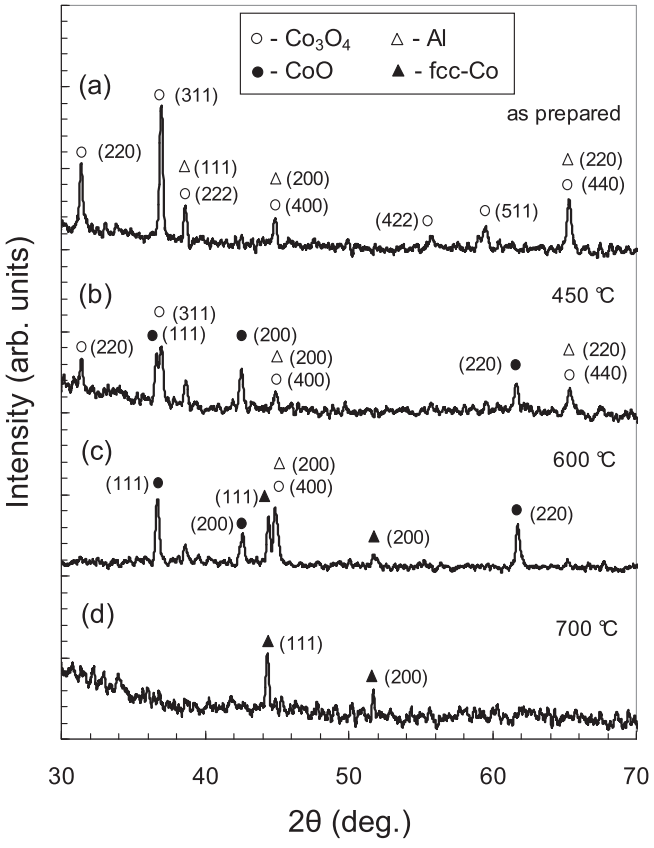

Fig. 2. Typical XRD patterns of the initial Al/Co_3O_4 bilayers (a), 450 °C (b) and the synthesized nanocomposites after annealing at 600 °C (c), 700 °C (d).

percolation threshold. Above 700 °C the electrical resistance only weakly depended on the annealing temperature and it is assumed that both the reaction between Al and Co_3O_4 and the reaction between Al and CoO had been completed at 700 °C. As the temperature decreased from 700 °C to room temperature the resistance R decreased nonlinearly (Fig. 1c) and the lnR against T^{-1} plot is given in the inset of Fig. 1c. A logarithm of R plot was found to be linearly proportional to T^{-1} (T_0 = 120 K, E_a = 0.01 eV) below 250 °C. This result shows a characteristic of the granular composite which is attributed to the thermally activated conduction mechanism that is typical for most metal granular films at these temperatures [31]. The deviation from linear proportionality in the (700 °C - 250 °C) temperature range is most likely the result of post-reaction processes continued in the synthesized Co-Al_2O_3 samples.

3.4. TEM characterizations

Fig. 3 shows a typical TEM image and the selected area electron diffraction pattern (SAED) after annealing at 700 °C. The average atomic number for the Al_2O_3 phase is lower than the atomic number of Co thus the Al_2O_3 region appears brighter than the Co region on the TEM image (Fig. 3a). The TEM observations (Fig. 4a) indicate that the Co nanoparticles have an out-of-round shape with a grain size of 20–120 nm and good uniformity in the reaction product. It follows from the histogram that the average diameter of the Co nanoparticles is ~40 nm (Inset in Fig. 3a). This diameter is consistent with the average size of the Co grains determined by XRD. It is important to bear in mind that the constituent parts of the Co nanoparticles have sizes below 20 nm, which are not observed in the TEM image. The d-spacing obtained from the SAED pattern (Fig. 3b) indicates the presence of an additional $AlCo_2O_4$ phase besides the expected hcp-Co, fcc-Co and α-Al_2O_3 phases, as illustrated in Table 1. However, $CoAl_2O_4$ is not visible in XRD patterns (Fig. 2c, d). This corroborates the incomplete reduction of Co by the Al during reaction (1) and the elemental profiles determined by the EDX scan (Fig. 4b) are indicative of a possible partial interdiffusion between the Co and Al_2O_3 which forms $Co_{1+x}Al_{2-x}O_4$ spinel-type solid solutions. Atomic rearrangements can take place during the annealing process at 700 °C to facilitate the formation of the $AlCo_2O_4$ shell at the Co/Al_2O_3 interface.

3.5. XPS studies

XPS spectra were measured to further confirm the chemical state of Co and Al in the synthesized Co-Al_2O_3 films. Fig. 5 shows the typical Al 2p and Co 2p photoelectron spectra of the Co-Al_2O_3 film after etching with Ar^+ ions to remove an oxidized surface layer. The main Co $2p_{3/2}$ peak is centered at the binding energy of 778.7 eV corresponding to metallic Co [32], whereas the maximum at 782.1 eV may be attributed to the Co atoms in $CoAl_2O_4$ [33,34] (Fig. 5b). There are no peaks at 780.4 eV and 779.7 eV, indicating the absence of the CoO and Co_3O_4 phases [33]. The Al 2p peak is located at 74.9 eV, suggesting that all Al atoms are oxidized [33] (Fig. 5a). We can propose therefore that the intermediate spinel $CoAl_2O_4$ layer arises during the reaction between the Co_3O_4 and Al films. At the same time, the Al to Co atomic ratios found using XPS are as high as 15–20 probably due to the Co-bearing phases from the Co/$CoAl_2O_4$ core-shell clusters or particles exposing a low surface area in the Al_2O_3 matrix as opposed to continuous films. The volume of the spinel shells containing up to 40% of Co atoms in a non-magnetic state appears to be comparable with that of metallic Co. The existence of the $CoAl_2O_4$ phase was found after ion implantation of Co into an (0001)Al_2O_3 substrate [34], with (CoNi)Al_2O_4 and $CoAl_2O_4$ spinel phases existing in the Al_2O_3-(CoNi) [35] and Al_2O_3–Co cermets [36], respectively, prepared by combustion synthesis in a thermal explosion mode.

Thus, the final synthesized products consist of Co nanoparticles enveloped by $AlCo_2O_4$ layers dispersed in an Al_2O_3 matrix.

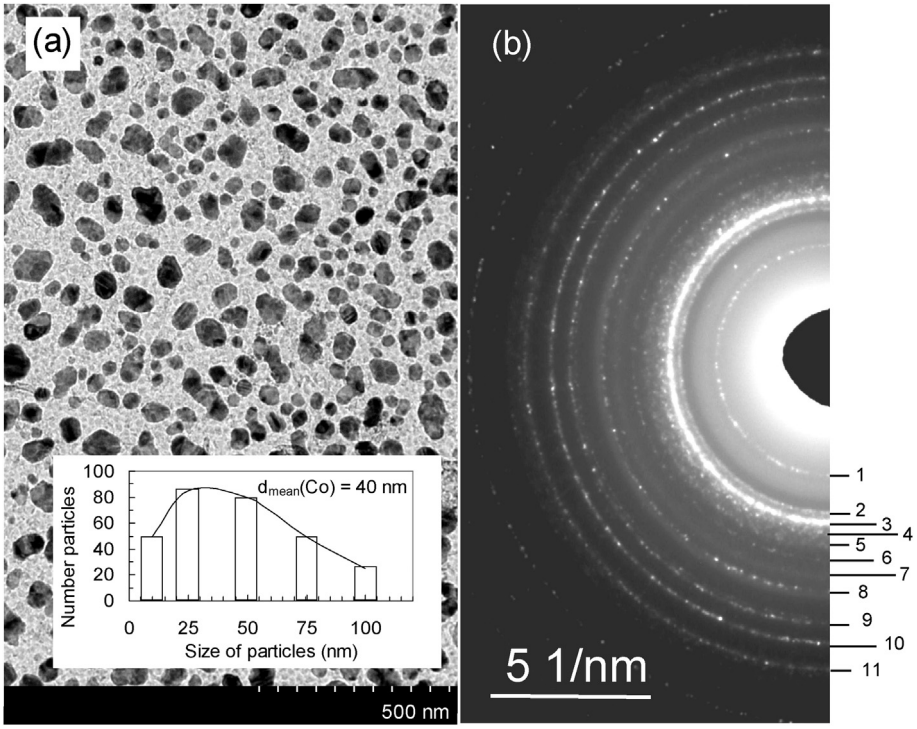

Fig. 3. TEM image (a) of Co nanoparticles embedded in the Al_2O_3 matrix and histogram of Co nanoparticle size distribution obtained from the TEM image (a) and (b) electron diffraction pattern of the Co-Al_2O_3 film after annealing at 700 °C.

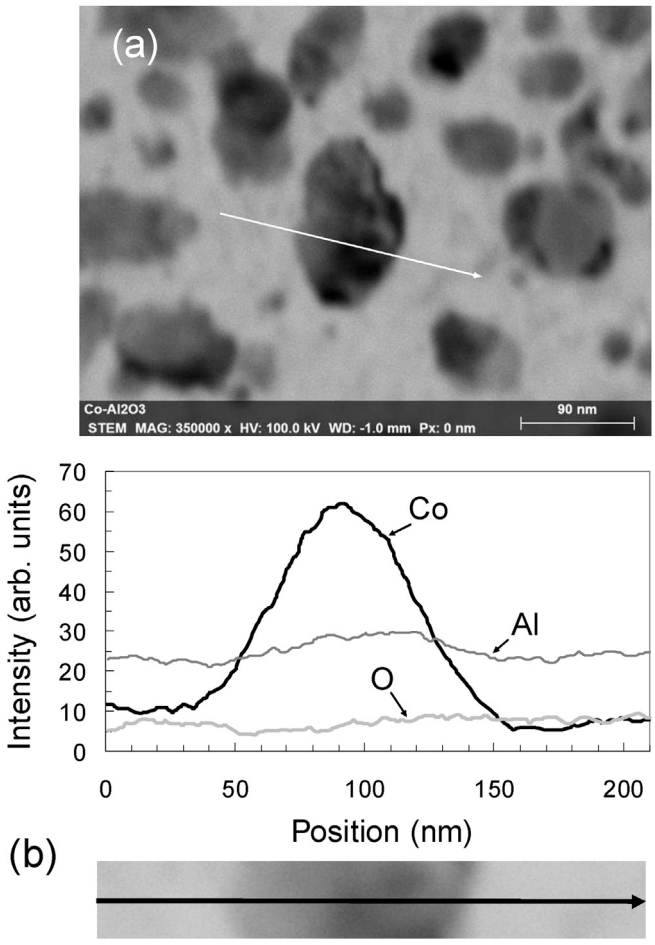

Fig. 4. TEM image of (a) Co nanoparticles embedded in the Al_2O_3 matrix. (b) The TEM image and EDS profiles of concentrations of Co, Al, and O along the line across the particle in a nanocomposite Co-Al_2O_3 film after annealing at 700 °C.

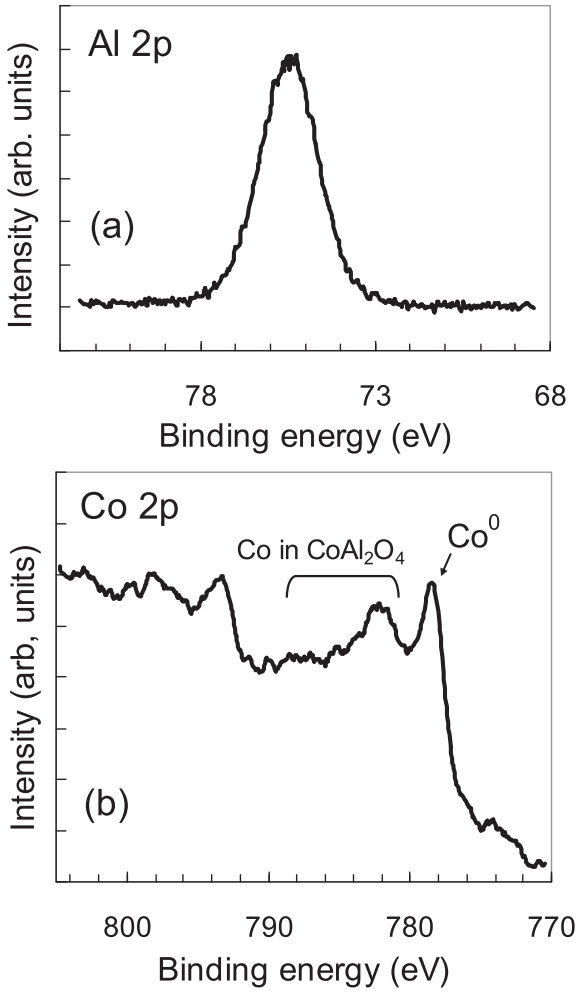

Fig. 5. (a) XPS of Al 2p peak and (b) Co 2p peaks for the synthesized nanocomposite Co-Al_2O_3 film after annealing at 700 °C.

Table 1
Indexing the diffraction reflections in Fig. 3b.

Rings	α-Al_2O_3	fcc-Co	hcp-Co	$CoAl_2O_3$
1				(220)
2	(104)		(100)	(311)
3	(113)	(111)	(002)	(400)
4			(101)	
5	(024)	(200)		
6	(116)			(422)
7	(211)			(511)
8	(214)			(440)
9	(1010)	(220)	(110)	(533)+(622)
10	(220)			(444)
11		(311)	(201)	(642)

3.6. Magnetic properties

After annealing at 700 °C more than 60% of Co was reduced in the Co-Al_2O_3 nanocomposites and it therefore had a saturation magnetization of ~220 emu/cm^3 (inset in Fig. 1b). The occurrence of hysteresis loops confirms that the size of the Co nanoparticles in the Co-Al_2O_3 films was larger than the superparamagnetic critical size (on the order of 20 nm) for Co nanoparticles [37]. The measured hysteresis loop looks very much like the Stoner–Wolfarth curve, which describes the hysteresis loop of a random assembly of noninteracting single-domain ferromagnetic particles with uniaxial anisotropy and possesses the ratio $M_r/M_S = 0.5$ (where M_r is magnetic remanence) [38]. The hysteresis loops of the synthesized Co-Al_2O_3 nanocomposites have a ratio M_r/M_S ~0.3 and the magnetization reached saturation M_S only in applied fields up to H_{sat} ~1.5 kOe (inset in Fig. 1b). This clearly indicates that, together with the ferromagnetic Co nanoparticles, a significant amount of superparamagnetic Co nanoparticles and frustrated spins at the enveloped $AlCo_2O_4$ layers contribute to the decrease of the remnant magnetization and strongly increase the high applied saturation magnetic field H_{sat} ($H_{sat} >> H_C$). The superparamagnetic critical size for the Co nanoparticles is on the order of 20 nm [37]. The rough estimate from the histogram (inset in Fig. 3a) of the relative value of the superparamagnetic Co nanoparticles is ~10%. An important point is that the histogram is presented for a film thickness of 50 nm and may be different from the histograms for film thicknesses of 300–400 nm, which were used for the magnetic and electrical resistance investigations.

It is known that the magnetocrystalline anisotropy constants $K_1^{hcp} = 4 \times 10^5$ J/m^3 [39], $K_1^{fcc} = 0.7 \times 10^5$ J/m^3 [40,41] and the exchange stiffness A_{ex} in ferromagnetic Co films obtained by different methods do not exceed 3×10^{-11}J/m [42]. Therefore, the exchange length $L_{ex} = (A_{ex}/K_1)^{1/2}$ is below 20 nm, which is less than the interparticle distances for most Co nanoparticles observed in Fig. 3b and only a small part of Co nanoparticles are exchange-coupled with each other through the Al_2O_3 matrix.

In summary, synthesized Co-Al_2O_3 nanocomposites may be

present as an assembly of noninteracting Co nanoparticles below the percolation threshold (dielectric regime) embedded into an insulating Al_2O_3 matrix.

4. Discussion

After annealing above 450 °C x-ray diffraction shows the start of CoO formation (Fig. 2b) due to reaction (3) and above 550 °C the Co_3O_4 is completely transformed into CoO (Fig. 2c). It follows that above the initiation temperature T_{in} ~500 °C the proposed reaction mechanism is the simultaneous existence of competing (1), (3), (4) reactions, where reaction (3) is the dominate reaction. Therefore, the formation of the insulating Al_2O_3 phase by the (1) and (4) reactions is low and results in an insignificant growth of the electric resistance during the (500 °C - 600 °C) temperature interval (Fig. 1c). The sharp growth of the electric resistance (Fig. 1c) and the degree of the Co reduction (Fig. 1b) strongly suggest that reaction (4) is the dominate reaction above 600 °C. Intermediate reactions often accompany the main reaction in different thermite nanoenergetic composites including the reaction between Co_3O_4 and Al [43–45]. Recently we have showed that intermediate reactions were also present in the thermite reaction between Co_3O_4 and Zr films [18].

Magnetic, XPS and TEM studies show the existence of $CoAl_2O_4$ shells enveloping Co nanoparticles, which contain up 40% Co atoms. If we assume that the average size of Co nanoparticles is 40 nm, the crude estimation of the $CoAl_2O_4$ shell thickness doesn't exceed 20 nm. However, the real value of this thickness can be low because of the partial dissolution of Co in the Al_2O_3 matrix.

As is known, thin film solid state reactions are characterized by the initiation temperature T_{in} and the first phase arising at the film interface when the temperature of a sample T_S exceeds T_{in} ($T_S > T_{in}$) [46–50]. When a reaction starts, many characteristics begin change radically, therefore T_{in} is easy to find using electrical resistance, magnetization, transparence etc as a function of temperature. In this work, T_{in} was identified using electrical resistance and degree of Co reduction as function of temperature (Fig. 1b, c). In nanoenergetic materials the initiation temperatures may be determined from the curves of the differential thermal analysis (DTA) and differential scanning calorimetry (DSC), as the temperature at which heat release starts. For Co_3O_4/Al nanothermite composites, the value of T_{in} ~500 °C, obtained from DTA and DSC plots [43–45] is in good agreement with the initiation temperature T_{in} ~500 °C of the (1), (4) reactions (Fig. 1b, c). It follows from this that, at nanoscale, the initiation temperature T_{in} ~500 °C is the characteristic temperature of the start of the synthesis of the Co-Al_2O_3 nanocomposites, and does not depend on the fabrication techniques, the morphology nor the size of the Al/Co_3O_4 nanoenergetic materials. The X-ray diffraction patterns and magnetic properties do not change over 6 months, which proposes good chemical stability of the synthesized Co-Al_2O_3 samples at room temperature.

Based on all the above, it can be concluded that the final product of the thermite reaction in the Al/Co_3O_4 thin films contained Co nanoparticles above the superparamagnetic critical size enveloped by $CoAl_2O_4$ shell and separated by Al_2O_3 dielectric gaps below the percolation threshold. The particle size of the Co during the thermite reaction in the Al/Co_3O_4 thin films strongly depended on the experimental conditions, such as the heating rate and the annealing time. Therefore, the choice of heat treatment regime determines the structural and magnetic properties of the nanocomposite Co-Al_2O_3 thin films.

5. Conclusion

In summary, Co-Al_2O_3 ferromagnetic nanocomposites were successfully synthesized by a thermite reaction between Al and Co_3O_4 thin films. The starting Al/Co_3O_4 films were obtained by the oxidation of the Co films in air and the sequential deposition of Al layers. At annealing temperatures above 400 °C up to 500 °C a partial transformation of the Co_3O_4 to CoO occurred and there was no reaction of the Co_3O_4 and CoO with Al. However, above the initiation temperature T_{in} ~500 °C the reaction started simultaneously between both Co_3O_4 and Al and CoO and Al and was completed after annealing at 700 °C. The final microstructure of the Co-Al_2O_3 nanocomposite films contained Co nanoparticles with an average size ~40 nm enveloped by $CoAl_2O_4$ shell dispersed homogeneously in the insulating Al_2O_3 matrix. The magnetic characterization indicated that the hysteresis loop shape, the magnetization saturation and the coercive force depend on the chemical interactions of the Co nanoparticles with the enveloped $CoAl_2O_4$ shell. It has been proposed that the initiation temperature T_{in} ~500 °C is the control temperature of the Co-Al_2O_3 nanocomposite synthesis.

Acknowledgements

This study was supported by the Russian Foundation for Basic Research (grants #16-03-00069, #15-02-00948, and #16-32-00302 мол_а), by Russian Foundation for Basic Research, Government of Krasnoyarsk Territory, Krasnoyarsk Region Science and Technology Support Fund to the research project #16-42-243059 р_мол_а and #16-42-243006 р_мол_а, by the Council for Grants of the President of the Russian Federation (SP-317.2015.1, SP-1373.2016.3). The XPS and TEM studies were carried out using the facilities of the Performance Service at Krasnoyarsk Scientific Center.

References

[1] E.L. Dreizin, Metal-based reactive nanomaterials, Prog. Energy Combust. Sci. 35 (2009) 141–167.
[2] X. Zhou, M. Torabi, J. Lu, R. Shen, K. Zhang, Nanostructured energetic composites: synthesis, ignition/combustion modeling, and applications, ACS Appl. Mater. Interfaces 6 (2014) 3058–3074.
[3] A.S. Rogachev, A.S. Mukasyan, Combustion of heterogeneous nanostructural systems (Review), Combus. Explos. Shock Waves 46 (2010) 243–266.
[4] M. Comet, C. Martin, M. Klaumünzer, F. Schnell, D. Spitzer, Energetic nanocomposites for detonation initiation in high explosives without primary explosives, Appl. Phys. Lett. 107 (2016), 243108–1-243108-4.
[5] G. Zheng, W. Zhang, R. Shen, J. Ye, Z. Qin, Y. Chao, Three-dimensionally ordered macroporous structure enabled nanothermite membrane of Mn_2O_3/Al, Sci. Rep. 6 (2016) 22588, http://dx.doi.org/10.1038/srep22588.
[6] T. Zhang, Z. Ma, G. Li, Z. Wang, B. Zhao, Y. Luo, Electrostatic interactions for directed assembly of high performance nanostructured energetic materials of Al/Fe_2O_3/multi-walled carbon nanotube (MWCNT), J. Solid State Chem. 237 (2016) 394–403.
[7] D.P. Adams, Reactive multilayers fabricated by vapor deposition: a critical review, Thin Solid Films 576 (2015) 98–128.
[8] T.P. Weihs, Fabrication and characterization of reactive multilayer films and foils, in: K. Barmak, K.R. Coffey (Eds.), Metallic Films for Electronic, Optical and Magnetic Applications: Structure, Processing and Properties, Woodhead Publishing, Swaston, UK, 2014, pp. 160–243. Chap. 6 (Invited Review).
[9] A.S. Rogachev, Exothermic reaction waves in multilayer nanofilms, Russ. Chem. Rev. 77 (2008) 21–37.
[10] C. Yu, W. Zhang, R. Shen, X. Xu, J. Cheng, J. Ye, Z. Qin, Y. Chao, 3D ordered macroporous NiO/Al nanothermite film with significantly improved higher heat output, lower ignition temperature and less gas production, Mater. Des. 110 (2016) 304–310.
[11] L.-Z. Lin, X.-L. Cheng, B. Ma, Reaction characteristics and iron aluminides products analysis of planar interfacial Al/α-Fe_2O_3 nanolaminate, Comput. Mater. Sci. 127 (2017) 29–41.
[12] K.J. Blobaum, M.E. Reiss, J.M. Plitzko, T.P. Weihs, Deposition and characterization of a self-propagating uO_x/$AlCuO_x$/Al hermite reaction in a multilayer foil geometry, J. Appl. Phys. 94 (2003) 2915–2922.
[13] J. Kwon, J.M. Ducéré, P. Alphonse, M. Bahrami, M. Petrantoni, J.-F. Veyan, C. Tenailleau, A. Estève, C. Rossi, Y.J. Chabal, Interfacial chemistry in Al/CuO reactive nanomaterial and its role in exothermic reaction, ACS Appl. Mater. Interfaces 5 (2013) 605–613.
[14] G.C. Egan, E.J. Mily, J.-P. Maria, M.R. Zachariah, Probing the reaction dynamics

of thermite nanolaminates, J. Phys. Chem. C 119 (2015) 20401–20408.
[15] S. Fu, Y. Zhu, D. Li, P. Zhua, B. Hu, Y. Ye, R. Shen, Deposition and characterization of highly energetic Al/MoOx multilayer nano-films, Eur. Phys. J. Appl. Phys. 64 (2013), 30301–1-30301-5.
[16] V.G. Myagkov, I.A. Tambasov, O.A. Bayukov, V.S. Zhigalov, L.E. Bykova, Yu.L. Mikhlin, M.N. Volochaev, G.N. Bondarenko, Solid state synthesis and characterization of ferromagnetic nanocomposite Fe-In_2O_3 thin films, J. Alloys Compd. 612 (2014) 189–194.
[17] V.G. Myagkov, L.E. Bykova, O.A. Bayukov, V.S. Zhigalov, I.A. Tambasov, S.M. Zharkov, A.A. Matsynin, G.N. Bondarenko, Solid state synthesis and characterization of Fe–ZrO_2 ferromagnetic nanocomposite thin films, J. Alloys Compd. 636 (2015) 223–228.
[18] V.G. Myagkov, V.S. Zhigalov, L.E. Bykova, S.M. Zharkov, A.A. Matsynin, M.N. Volochaev, I.A. Tambasov, G.N. Bondarenko, Thermite synthesis and characterization of Co-ZrO_2 ferromagnetic nanocomposite thin films, J. Alloys Compd. 665 (2016) 197–203.
[19] Y. Wang, L. Wang, H. Zhang, Z. Zhong, D. Peng, F. Ye, F. Bai, Investigation of FeCo-Ti-O nanogranular films with tunable permeability spectrum, J. Alloys Compd. 667 (2016) 229–234.
[20] H. Bakkali, M. Dominguez, X. Batlle, A. Labarta, Equivalent circuit modeling of the ac response of Pd-ZrO_2 granular metal thin films using impedance spectroscopy, J. Phys. D. Appl. Phys. 48 (2015), 335306–1-335306-7.
[21] M.A.S. Boff, B. Canto, R. Hinrichs, L.G. Pereira, F. Mesquita, J.E. Schmidt, G.L.F. Fraga, Electrical current influence on resistance and localization length of a Co–Al_2O_3 granular thin film, Phys. B 406 (2011) 4304–4306.
[22] H. Bakkali, M. Dominguez, Differential conductance of Pd-ZrO_2 thin granular films prepared by RF magnetron sputtering, Europhys. Lett. 104 (2013), 17007–1-17007-4.
[23] C. Chen, O. Kitakami, S. Okamoto, Y. Shimada, Surface anisotropy in giant magnetic coercivity effect of cubic granular FeCo/SiO_2 and NiCo/SiO_2 films: a comparison with Néel's theory, J. Appl. Phys. 86 (1999) 2161–2165.
[24] Z. Konstantinovic, M.G. del Muro, M. Varela, X. Batlle, A. Labarta, Particle growth mechanisms in Ag-ZrO_2 and Au–ZrO_2 granular films obtained by pulsed laser deposition, Nanotechnology 17 (2006) 4106–4111.
[25] J. Varalda, W.A. Ortiz, A.J.A. de Oliveira, B. Vodungbo, Y.-L. Zheng, D. Demaille, M. Marangolo, D.H. Mosca, Tunnel magnetoresistance and Coulomb blockade in a planar assembly of cobalt nanoclusters embedded in TiO_2, J. Appl. Phys. 101 (2007), 014318–1-014318-4.
[26] S.V. Komogortsev, E.A. Denisova, R.S. Iskhakov, A.D. Balaev, L.A. Chekanova, Yu.E. Kalinin, A.V. Sitnikov, Multilayer nanogranular films $(Co_{40}Fe_{40}B_{20})_{50}$(-$SiO_2)_{50}$/α-Si:H and $(Co_{40}Fe_{40}B_{20})_{50}(SiO_2)_{50}/SiO_2$: magnetic properties, J. Appl. Phys. 113 (2013) (2013), 17C105-1-17C105-3.
[27] A.A. Timopheev, I. Bdikin, A.F. Lozenko, O.V. Stognei, A.V. Sitnikov, A.V. Los, N.A. Sobolev, Superferromagnetism and coercivity in Co-Al_2O_3 granular films with perpendicular anisotropy, J. Appl. Phys. 111 (2012), 123915–1-123915-7.
[28] J. Okabayashi, S. Kono, Y. Yamada, K. Nomura, Fabrication and magnetic properties of Fe and Co co-doped ZrO_2, AIP Adv. 1 (2011), 042138–1-042138-6.
[29] H. Fujimori, S. Mitani, S. Ohnuma, Tunnel-type GMR in metal-nonmetal granular alloy thin films, Mater. Sci. Eng. B 31 (1995) 219–223.
[30] K. Yakushiji, F. Ernult, H. Imamura, K. Yamane, S. Mitani, K. Takanashi, S. Takahashi, S. Maekawa, H. Fujimori, Enhanced spin accumulation and novel magnetotransport in nanoparticles, Nat. Mater. 4 (2005) 57–61.
[31] C.A. Neugebauer, M.B. Webb, Electrical conduction mechanism in ultrathin, evaporated metal films, J. Appl. Phys. 33 (1962) 74–82.
[32] C.J. Powell, Recommended Auger parameters for 42 elemental solids, J. Electron Spectros. Relat. Phenom. 185 (2012) 1–3.
[33] X. Duan, M. Pan, F. Yu, D. Yuan, Synthesis, structure and optical properties of CoAl2O4 spinel nanocrystals, J. Alloys Compd. 509 (2011) 1079–1083.
[34] J.-K. Lee, M.F. Hundley, J.D. Thompson, R.K. Schulze, H.S. Jung, J.A. Valdez, M. Nastasi, X. Zhang, Magnetic anisotropy study of ion-beam synthesized cobalt nanocrystals, Appl. Phys. Lett. 89 (2006), 182502–1-182502-3.
[35] T. Lu, Y. Pan, Synthesis of Al_2O_3-(Co,Ni) cermets via thermal explosion method, Mater. Manuf. Process. 26 (2011) 1288–1292.
[36] T. Lu, Y. Pan, Combustion synthesis of ferromagnetic Al_2O_3-based cermets in thermal explosion mode, J. Mater. Sci. 45 (2010) 5923–5928.
[37] A.I. Gusev, A.A. Rempel, Nanocrystalline Materials, Cambridge International Science Publishing, 2004, p. 351.
[38] E.C. Stoner, E.P. Wohlfarth, A mechanism of magnetic hysteresis in heterogeneous alloys, Philos. Trans. R. Soc. Lond. Ser. A 240 (1948) 599–642.
[39] R.M. Bozorth, Ferromagnetism, IEEE Press, New York, 1978.
[40] J.A. Wolf, J.J. Krebs, G.A. Prinz, Growth and magnetic characterization of face centered cubic Co on (001) diamond, Appl. Phys. Lett. 65 (1994) 1057–1059.
[41] T. Suzuki, D. Weller, C.-A. Chang, R. Savoy, T. Huang, B.A. Gurney, V. Speriosu, Magnetic and magneto-optic-properties of thick face-centered-cubic Co single-crystal films, Appl. Phys. Lett. 64 (1994) 2736–2738.
[42] E. Girt, W. Huttema, O.N. Mryasov, E. Montoya, B. Kardasz, C. Eyrich, B. Heinrich, A.Yu. Dobin, O. Karis, A method for measuring exchange stiffness in ferromagnetic films, J. Appl. Phys. 109 (2011), 07B765-1-07B765-3.
[43] Z. Qiao, D. Xu, F. Nie, G. Yang, K. Zhang, Controlled facile synthesis, growth mechanism, and exothermic properties of large area Co_3O_4 nanowalls and nanowires on silicon substrates, J. Appl. Phys. 112 (2012), 014310–1-014310-9.
[44] D. Zhang, Q. Xiang, Electrophoretic fabrication of an Al-Co_3O_4 reactive nanocomposite coating and its application in a microignitor, Ind. Eng. Chem. Res. 55 (2016) 8243–8247.
[45] D. Xu, Y. Yang, H. Cheng, Y.Y. Li, K. Zhang, Integration of nano-Al with Co_3O_4 nanorods to realize high-exothermic core-shell nanoenergetic materials on a silicon substrate, Combust. Flame 159 (2012) 2202–2209.
[46] J.M. Poate, K.N. Tu, J.W. Mayer (Eds.), Thin Films-interdiffusion and Reaction, Willey-Interscience, New York, 1978, 578 pp.
[47] E.G. Colgan, A review of thin-film aluminide formation, Mater. Sci. Rep. 5 (1990) 1–44.
[48] R. Pretorius, C.C. Theron, A. Vantomme, J.W. Mayer, Compound phase formation in thin film structures, Crit. Rev. Solid. State Mater. Sci. 24 (1999) 1–62.
[49] R.W. Bené, First nucleation rule for solid-state nucleation in metal-metal thin-film systems, Appl. Phys. Lett. 41 (1982) 529–531.
[50] T. Laurila, J. Molarius, Reactive phase formation in thin film metal/metal and metal/silicon diffusion couples, Crit. Rev. Solid. State Mater. Sci. 28 (2003) 185–230.